Published in final edited form as:

Curr Biol. 2020 April 20; 30(8): 1477–1490.e3. doi:10.1016/j.cub.2020.02.023.

Critical roles of a RhoGEF-anillin module in septin architectural remodeling during cytokinesis

Xi Chen[1,3], **Kangji Wang**[1,3], **Tatyana Svitkina**[2], **Erfei Bi**[1,4,*]

[1]Department of Cell and Developmental Biology, Perelman School of Medicine, University of Pennsylvania, Philadelphia, PA 19104-6058

[2]Department of Biology, University of Pennsylvania, Philadelphia, PA 19104, USA

[3]These authors contribute equally

[4]Lead Contact

SUMMARY

How septin architecture is remodeled from an hourglass to a double ring during cytokinesis in fungal and animal cells remains unknown. Here, we show that during the hourglass-to-double ring transition in budding yeast, septins acquire a “zonal architecture” in which paired septin filaments that are organized along the mother-bud axis associate with circumferential single septin filaments, the RhoGEF Bud3, and the anillin-like protein Bud4 exclusively at the outer zones and with myosin-II filaments in the middle zone. Deletion of Bud3 or its Bud4-interacting domain, but not its RhoGEF domain, leads to a complete loss of the single filaments whereas deletion of Bud4 or its Bud3-interacting domain destabilizes the transitional hourglass, especially at the mother side, with partial loss of both filament types. Deletion of Bud3 and Bud4 together further weakens the transitional structure and abolishes the double ring formation, while causing no obvious defect in actomyosin ring constriction. This and further analyses suggest that Bud3 stabilizes the single filaments whereas Bud4 strengthens the interaction between the paired and single filaments at the outer zones of the transitional hourglass as well as in the double ring. This study reveals a striking zonal architecture for the transitional hourglass that pre-patterns two cytokinetic structures – a septin double ring and an actomyosin ring, and also defines the essential roles of a RhoGEF-anillin module in septin architectural remodeling during cytokinesis at the filament level.

*Corresponding author: For correspondence: Dr. Erfei Bi, Department of Cell and Developmental Biology, Perelman School of Medicine at the University of Pennsylvania, Philadelphia, PA 19104-6058, Tel: 215-573-6676, Fax: 215-746-8791, ebi@pennmedicine.upenn.edu.

AUTHOR CONTRIBUTIONS

X.C. and K.W. conducted the experiments and data analysis and wrote the first draft; T.S. advised PREM analysis and helped with data interpretation and manuscript preparation; E.B. conceptualized the study, analyzed the data, and wrote the manuscript.

DECLARATION OF INTERESTS

The authors declare no competing interests.

SUPPLEMENTAL INFORMATION

Supplemental information can be found online at

Graphical Abstract

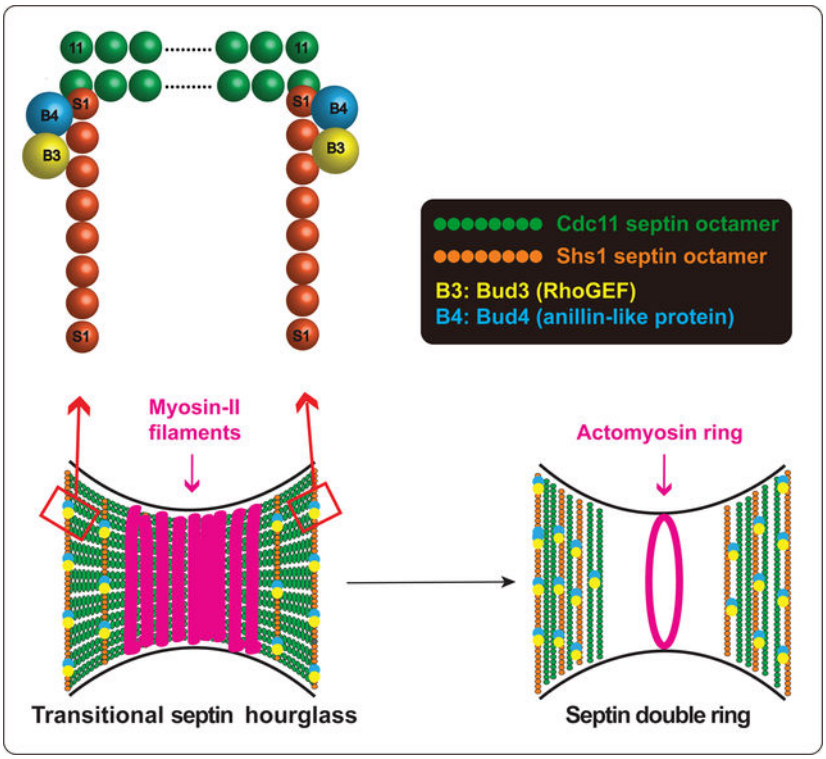

INTRODUCTION

Septins form distinct filamentous structures that act as a scaffold and/or diffusion barrier to carry out critical roles in diverse processes including cytokinesis, cell migration, membrane trafficking, and microbial infection [1–8]. During cytokinesis, septins stabilize the cell division site and also undergo dramatic architectural remodeling to allow fission. Such a remodeling event, in which one ring is remodeled into two, occurs in various organisms ranging from yeast to human [9–18]. In *Drosophila* S2 cells [19] and mammalian cells [16–18], septins form an hourglass-shaped structure during furrow ingression, which is then remodeled into a double ring during abscission. A similar transition occurs in the budding yeast *Saccharomyces cerevisiae* where septins at the bud neck (i.e. the cell division site) undergo an hourglass-to-double ring (HDR) transition at the onset of cytokinesis [9–11, 15]. In the fission yeast *Schizosaccharomyces pombe* [12, 13] and the filamentous fungi *Neurospora crassa* [20, 21] and *Aspergillus nidulans* [22, 23], septins also undergo a single ring-to-double ring transition at the onset of cytokinesis. Despite striking similarity of the septin architectural remodeling at the division site across species, the molecular mechanisms underlying this process remains largely unknown in any system.

We have previously shown using platinum-replica electron microscopy (PREM) [15] that the septin hourglass formed at the division site upon bud emergence in *S. cerevisiae* consists of paired septin filaments oriented along the mother-bud axis. This early hourglass develops into a “transitional hourglass” before cytokinesis in which the paired filaments are

intersected perpendicularly by periodic circumferential single septin filaments spaced by ~30 nm (the length of a single septin octamer) that can be seen underneath the paired filaments, whereas myosin-II filaments are present on the top and in the middle of paired-filament arrays. At the onset of cytokinesis, the transitional hourglass is remodeled into a double ring that contains a mixture of circumferential paired and single septin filaments. Together with live-cell imaging data, these findings suggest that septin remodeling during the HDR transition is regulated with a high spatial and temporal precision. However, these regulatory mechanisms are far from being understood.

A RhoGEF-anillin module plays important roles in coordinating actomyosin ring (AMR) assembly and septin recruitment to drive furrow ingression and stabilize the furrow shape, respectively, during cytokinesis in animal cells [19, 24–28]. A similar module in budding yeast is represented by the Cdc42-GEF Bud3 [29] and the anillin-like protein Bud4 [30]. Immunostaining data indicate that the endogenous Bud3 and Bud4 associate with the septin hourglass during mitosis and with the septin double ring during cytokinesis and cell separation [31, 32]. Both proteins interact with the septins through their central regions [33–36] and with each other through their C-terminal regions, which, in the case of Bud4, contains the anillin-homology (AH) and pleckstrin-hology (PH) domains [33, 34]. Genetic studies have also implicated Bud3 and Bud4 in septin organization [30, 33, 34, 37, 38]. Our previous analysis indicates that Bud4 is essential for maintaining the mother side of the double ring during cytokinesis [30]. However, it remains unknown how Bud3 and Bud4 affect the HDR transition at the architectural and filament level in vivo.

Using an integrative approach that combines yeast genetics, cell synchronization, quantitative live-cell imaging, and PREM coupled with immunogold labeling, we show here that the transitional septin hourglass possesses a zonal architecture, with Bud3 and Bud4 decorating the septin gauze at the outer zones while myosin-II filaments marking the middle zone. Bud3 and Bud4 play distinct and essential roles in the HDR transition, but are dispensable for AMR constriction.

RESULTS

The RhoGEF Bud3 and the anillin-like protein Bud4 localize to the outer zones of the transitional septin hourglass as well as the septin double ring

Previous studies suggest that the HDR transition involves filament disassembly [15, 30, 39–41] as well as assembly of the double ring instructed by unknown “spatial cues” at the ends of the hourglass [15]. We hypothesize that the RhoGEF Bud3 [29] and the anillin-like protein Bud4 [30] (Figure 1A) might function as the spatial cues, as both proteins associate with the septin hourglass during mitosis and with the septin double ring during and after cytokinesis [31, 32]. This pattern of localization is unique among the more than 120 bud neck-localized proteins in budding yeast [1, 2]. In addition, Bud4 is essential for maintaining the mother side of the double ring during cytokinesis, suggesting a role in the HDR transition [30].

To test the “spatial-cue” hypothesis, we first determined the precise timing and pattern of Bud3 and Bud4 localization in relation to the septin structures during the cell cycle.

Spinning-disk imaging of live cells expressing either Bud3-GFP or Bud4-GFP with Cdc3-mCherry (septin) (Figure 1B and Video S1) or with mRuby2-Tub1 (α-tubulin) (Figure S1 and Video S1) showed that both Bud3 and Bud4 began to localize to the preformed septin hourglass at the bud neck in S/G2, and then to the septin double ring during cytokinesis and cell separation (Figure S1). This result suggests that Bud3 and Bud4 are not required for early hourglass assembly, but might play a role in late hourglass and double ring formation. As expected, the septins (Cdc3-mCherry) displayed a stereotypical drop of 25–30% in intensity during the HDR transition (Figure 1C) [30, 38, 42]. In contrast, the levels of Bud3 and Bud4 remained fairly constant or even slightly increased during this period (Figure 1C). This data suggests that Bud3 and Bud4 might not associate with the septin filaments evenly throughout the hourglass. Indeed, analysis by super-resolution instant structured illumination microscopy (iSIM) revealed that both Bud3 and Bud4 localized first to the mother side of the septin hourglass, then to both ends of the hourglass, and, finally, co-localized with the septin double ring after the HDR transition (Figures 1D and 1E and Video S1). Together, these data indicate that Bud3 and Bud4 associate with the outer zones, but are less abundant or absent in the middle zone of the septin hourglass.

To determine the localization of Bud3 and Bud4 during the HDR transition at higher resolution, we used PREM coupled with immunogold-labeling [15]. Consistent with the iSIM data, we found that the gold particle-labeled Bud3 and Bud4 (Figure 1F) localized exclusively to the outer zones of a “transitional hourglass” [15] where the paired filaments running along the mother-bud axis (Figure 1F, **green**) were intersected by the circumferential single filaments at ~90° angle (Figure 1F, **orange**) [15]. In contrast, the middle portion of the transitional hourglass was occupied by myosin-II filaments (Figure 1F, **purple**) [15], but lacked the circumferential single filaments, and was not labeled by the Bud3 or Bud4 immunogold. As expected, Bud3 and Bud4 also associated with the septin filaments in the double ring (Figure 1F). These data define a striking “zonal architecture” for the transitional hourglass, and suggest that Bud3 and Bud4 are likely involved in the formation of the gauze structure.

Bud3 and Bud4 play distinct and essential roles in the septin hourglass-to-double ring transition, but are dispensable for actomyosin ring constriction

To define the specific roles of Bud3 and Bud4 in the HDR transition, we monitored septin behavior (Cdc3-GFP) in wild-type (WT), *bud3Δ*, *bud4Δ*, and *bud3Δ bud4Δ* cells by time-lapse microscopy. We found that the septin hourglass and double ring were fragmented at the onset of cytokinesis in every *bud3Δ* cell. The fragmented double ring was eventually disintegrated and migrated away from the division site (Figure 2A and Video S2). In *bud4Δ* cells, the mother side of the double ring was abolished, and the single ring at the daughter side lasted for less than 8 min, in contrast to the ~ 20 min duration for the double ring in WT cells (Figure 2A and Video S2) [30]. Strikingly, the septin double ring was nearly eliminated in *bud3Δ bud4Δ* cells; only a weak single ring was formed at the daughter side and disappeared quickly (Figure 2A and Video S2). Importantly, after cytokinesis, the assembly of a nascent septin ring, which would become an early hourglass upon bud emergence, formed normally in the double mutant (Figure 2A, **white arrow**, and Video S2), suggesting that Bud3 and Bud4 are dispensable for the assembly of early septin structures. This

conclusion is further supported by the fact that both proteins are expressed and begin to localize to the bud neck after S/G2 during the cell cycle [32, 43]. When the septin intensity at the bud neck was quantified against the background outside of the cell (Figure 2B), the intensity drops for different strains were 23% (WT), 35% (*bud3Δ*), 49% (*bud4Δ*), and 60% (*bud3Δ bud4Δ*), respectively, at the time of spindle break. Furthermore, the intensity drop occurred ~ 8 min earlier in the *bud3Δ bud4Δ* cells compared to the WT cells (Figure 2B). Taken together, these data indicate that Bud3 and Bud4 play important, but distinct roles, in the HDR transition.

To define the distinct roles of Bud3 and Bud4 at the architectural and filament levels, we performed PREM analysis. All of the transitional hourglass structures (n = 40) from WT cells arrested at the onset of cytokinesis consisted of longitudinal paired filaments oriented in parallel to the mother-bud axis (Figure 3A, **green**) and circumferential single filaments (Figure 3A, **orange**) [15]. The middle portion of the hourglass was devoid of the single filaments and was occupied by circumferential myosin-II filaments that were on top of the longitudinal paired filaments (Figure 3A, **uncolored region;** and Figure S2A). In *bud3Δ* cells, most of the transitional hourglass structures captured (61 out of 110) displayed "elongated" paired filaments at one side of the bud neck (Figure 3A, **right side**), which likely reflects fragmented transitional structures, as observed by time-lapse microscopy (Figure 2A and Video S2). Most importantly, none of these transitional structures (n = 110) contained the circumferential single filaments (Figures 3A and S2B), a defect that can be visualized only by PREM, not time-lapse, analysis. Thus, Bud3 is absolutely essential for the assembly and/or maintenance of the circumferential single filaments in the transitional hourglass. In *bud4Δ* cells, most of the transitional structures (59 out of 83) displayed a clear asymmetry, with one side having a gauze- or a partial gauze-like architecture, while the other side lacked single filaments and also had fewer paired filaments (Figure 3A, **orange**, and Figure S2B). The remaining transitional structures (24 out of 83) were disorganized on both sides, and contained no single filaments at either side. This is consistent with the preferential, but shortened, presence of septins at the daughter side of the bud neck in *bud4Δ* cells (Figure 2A and Video S2) [30]. Thus, Bud4 is required for the assembly and/or maintenance of both the paired and the single filaments in the transitional hourglass, especially at the mother side of the bud neck. Not surprisingly, very few septin transitional structures were recovered from *bud3Δ bud4Δ* cells. These structures were disorganized and contained no circumferential single filaments (Figure S2B). Together, these data indicate that Bud3 and Bud4 play distinct roles in the assembly of a transitional hourglass.

We also examined the double-ring structures from WT, *bud3Δ*, and *bud4Δ* cells. Note that only one side of the double ring was visualized in a majority of the cases. The other side was presumably separated from its cognate pair during unroofing. As expected, all the double ring halves (n = 74) from WT cells contained circumferential paired and single filaments that were connected by short bridges, often having a bulging appearance, at the intervals of 32.6 ± 5.0 nm (n = 153) - approximately the length of a septin octamer (Figures 3B and S3, **arrowheads**). In some cases (33 out of 74), an AMR was detected within the septin ring (Figures 3B, **arrows**). In *bud3Δ* cells, no intact double ring halves were observed. This is consistent with the absence of circumferential single filaments in the transitional hourglass,

which likely serve as precursors for the double ring. The presumed double ring fragments (n = 24) contained septin filaments with much less density than those from WT cells (Figures 3B and S2C). A few such structures (6 out of 24) were accompanied by a nearby AMR (Figures 3B). Despite this defect, the septin filaments in the double ring fragments were still connected by the bulging bridges at the intervals of 32.2 ± 5.2 nm (n = 63) (Figures 3B and S3, **arrowheads**). In *bud4Δ* cells, most of the double rings or their fragments were associated with an AMR (23 out of 29) (Figures 3B and S2C). Strikingly, the septin filaments in all the observed structures were no longer connected by the bulging bridges (Figures 3B and S3). These results suggest that Bud4 is required for crosslinking septin filaments in the double ring at the interval of a septin octamer. Together, these data demonstrate that Bud3 and Bud4 play distinct roles in the double ring assembly.

The zonal architecture of the transitional hourglass suggests that it pre-patterns two cytokinetic structures – a septin double ring and an AMR. Both structures are simultaneously generated from remodeling of the transitional hourglass at the onset of cytokinesis, and act in concert to promote cytokinesis [30]. The data described above demonstrate that Bud3 and Bud4 play essential roles in converting the gauze-like structure at the outer zones of the transitional hourglass into a septin double ring. In contrast, we found that the constriction of the AMR, marked by Myo1-GFP (the sole myosin-II heavy chain in budding yeast) [44, 45], appeared largely normal in *bud3Δ*, *bud4Δ*, or *bud3Δ bud4Δ* cells (Figures S4A and S4B; and Video S3). Thus, Bud3 and Bud4 are dispensable for AMR constriction. This observation also suggests that the paired septin filaments in the transitional hourglass, especially those beneath the myosin-II filaments in middle zone, are sufficient for scaffolding AMR assembly, and that cell cycle-triggered removal of these septin filaments allows the AMR to be anchored to the PM and initiate its constriction. Indeed, the mitotic exit network-controlled displacement of septins at the division site is required for AMR constriction [46]. Taken together, these data suggest that Bud3 and Bud4 play essential roles in the HDR transition, but not in AMR assembly and constriction.

Bud3 targets to the division site via both Bud4-dependent and -independent mechanisms

Bud3 and Bud4 are known to interact with each other [35, 47], as well as with septins [33, 34, 36]. To understand their specific roles in the HDR transition, we must understand their interplay at the division site during the cell cycle. Towards this goal, we found that in the absence of Bud4, the accumulation of Bud3-GFP at the division site dropped by ~55% (see Methods for details) in comparison to its intensity in WT cells before the HDR transition (Figures 4A and 4B and Video S4), indicating that Bud3 possesses both Bud4-dependent and –independent mechanisms for its targeting to the bud neck before the HDR transition. The Bud4-dependent mechanism is likely mediated by its direct interaction with Bud4 whereas the Bud4-independent mechanism is likely mediated by its interactions with the septins and the PM [33–35]. These data also suggest that Bud3 is able to interact with the paired septin filaments in the early hourglass (without circumferential single filaments) [15] before the HDR transition. During the HDR transition, Bud3-GFP was essentially lost at the division site in *bud4Δ* cells, except for a weak signal at the daughter side of the bud neck (Figures 4A and 4B and Video S4). This pattern of Bud3-GFP localization was similar to that of Cdc3-GFP localization in *bud4Δ* cells during the HDR transition (Figures 2A and 2B

and Video S2), suggesting that the further loss of Bud3 localization in *bud4Δ* cells during the HDR transition is due to the loss of septin structures caused by the absence of Bud4. Thus, Bud4 may retain Bud3 at the division site via a direct interaction as well as indirectly via its role in septin organization. In contrast, deletion of *BUD3* did not appreciably change the overall spatiotemporal profile of Bud4-GFP at the division site, but caused Bud4-GFP signal to fragment and migrate away from the division site during the HDR transition (Figures 4C and 4D and Video S4) [47]. This phenotype is remarkably similar to the septin behavior in *bud3Δ* cells (Figure 2A and Video S2), suggesting that Bud4 can associate with the septins independent of Bud3 [47]. Taken together, these results indicate that despite the overall similarity in localization pattern, Bud3 and Bud4 regulate each other's behavior in distinct ways. Bud4 closely associates with septins and partially controls Bud3 localization whereas Bud3 is largely dispensable for Bud4 localization at the bud neck.

The Bud4-interacting domain, but not the RhoGEF domain, of Bud3 is essential for the assembly of the single filaments in the transitional hourglass

We then analyzed how specific domains in Bud3 and Bud4 mediate their localizations to the bud neck and contribute to their roles in the HDR transition. We first examined the possibility that Bud3 regulates the HDR transition through its GEF activity towards Cdc42, which is thought to be important for spatially linking the division site to the next polarization or budding site [29]. However, precise deletion of the coding sequence for the RhoGEF domain (aa259–442) of Bud3 at the endogenous locus affected neither the Bud3 localization nor the HDR transition during the cell cycle (Figures S5A and S5B). The zonal architecture of the transitional hourglass was also properly maintained (32 out of 32 structures examined) (Figures 5A and 5B). Thus, the GEF domain of Bud3 is not required for its localization or septin remodeling.

In contrast, deletion of the Bud4-interacting domain (B4ID, aa1221–1636) in Bud3 caused nearly ~35% drop in its localization to the bud neck before the HDR transition (Figure S6A and S6B), similar to Bud3 localization in *bud4Δ* cells (~55% drop) (Figures 4A and 4B). Thus, the Bud4-dependent localization of Bud3 before the HDR transition is mainly mediated by B4ID. Unlike the near-complete loss of Bud3-GFP at the bud neck in *bud4Δ* cells during the HDR transition (Figures 4A and 4B), the level of Bud3-B4IDΔ-GFP at the bud neck remained the same before and during the HDR transition (Figure S6A and S6B). This observation could be explained by the fact that the septin structures were retained much better at the division site during the HDR transition in *bud3-B4IDΔ* cells (Figure S6A and S6B) than in *bud4Δ* cells (Figures 4A and 4B), presumably due to the presence of Bud4 in the *bud3-B4IDΔ* cells that could stabilize the septin structures. This was indeed the case, as the septin double ring was nearly abolished in *bud3-B4IDΔ bud4Δ* cells and, consequently, Bud3-B4IDΔ-GFP failed to localize to the bud neck during the HDR transition (Figure S6A and S6B). Thus, the Bud4-stabilized septin structures might help retain Bud3-B4IDΔ at the division site during the HDR transition via an interaction between the septin-association domain (SAD) in Bud3 and the septins (Figure 1A) [33]. This interaction could, in turn, stabilize the septin structures at the bud neck, as their fragmentation during the HDR transition was much less pronounced in *bud3-B4IDΔ* cells than in *bud3Δ* cells (Figures 2A and S6A). Surprisingly, the localization of Bud3-B4IDΔ to the bud neck was also nearly

abolished in *bud4Δ* cells before the HDR transition, despite the presence of abundant septins at the bud neck (Figure S6A and S6B). The underlying reason remains unknown, although it is possible that the altered architecture of the septin hourglass in *bud4Δ bud3-B4IDΔ* cells might prevent its interaction with the SAD in Bud3-B4IDΔ. Collectively, these data indicate that the B4ID of Bud3 plays a role in its neck localization as well as in septin organization.

Indeed, the *bud3-B4IDΔ* cells displayed more rapid disassembly of the septin double ring at the mother side than at the daughter side (Figure S6A and S6B). This phenotype is similar, but much milder than that of the *bud4Δ* cells (Figures 2A and 2B). Nonetheless, these data suggest that the interaction of Bud3 with Bud4 is preferentially needed for maintaining the mother side of the septin double ring. Remarkably, PREM analysis showed that the circumferential single filaments in the transitional hourglass were completely abolished (44 out of 44 structures examined) (Figures 5A and 5C), indicating that the B4ID of Bud3 is essential for the assembly and/or maintenance of the single filaments in the transitional hourglass.

The AH and PH domains of Bud4 are critical for the assembly and stability of the transitional hourglass

Similarly, we examined different domains of Bud4 for their roles in Bud4 and Bud3 localization as well as in the HDR transition. As expected, deletion of the septin-interacting domain (SID, aa623–774) of Bud4 [33–36] reduced its localization to the bud neck throughout the cell cycle (dropped by ~34% and 24% at the time points −14 and +4, respectively) (Figures 6A and 6B), presumably due to its decreased interaction with the septins. As the neck localization of Bud3 partially depends on Bud4, not surprisingly, this localization was also reduced in *bud4-SIDΔ* cells (dropped by ~26% and 24% at the time points −14 and +4, respectively) (Figures S7A and S7B). The septins were able to undergo the HDR transition in *bud4-SIDΔ* cells, although the septin intensities were reduced before and during the HDR transition, and the mother side of the double ring was hardly detectable (Figures 6A, 6B, S7A, and S7B). This destabilization of septin structures at the bud neck is presumably caused by the reduced binding of Bud4 and Bud3 to the septins in *bud4-SIDΔ* cells, which likely acts as a stabilizing force during the HDR transition.

We then deleted the C-terminal fragment (aa1067–1447) of Bud4, which contains the AH-PH domains (Figure 1A) [for simplicity, this truncated allele is referred to as *bud4-(AH-PH)Δ* hereafter]. Bud4-(AH-PH)Δ displayed a dramatic loss of neck localization (dropped by ~56% at the time point −14) before the HDR transition with no apparent effect on the hourglass shape and intensity (Figures 6A and 6B). The localization of Bud3 to the bud neck was also dramatically reduced in *bud4-(AH-PH)Δ* cells (dropped by ~48% at the time point −14) (Figures S7A and S7B). This is not surprising, as the AH-PH domains of Bud4 are known to interact with Bud3 (Figure 1A) [34, 35]. Thus, the AH-PH domains play a major role in the localization of Bud4 to the bud neck before the HDR transition, which, in turn, affects Bud3 accumulation at the bud neck. However, these domains are largely dispensable for the maintenance of septins at the bud neck before the HDR transition.

Strikingly, the localization of Bud4-(AH-PH)Δ at the bud neck increased dramatically during the HDR transition, and this increase was accompanied by a positional shift of Bud4-(AH-

PH)Δ, together with the septins, from the mother side to the daughter side (Figure 6A, **arrows** and Figure 6B). The shift was also manifested by the sudden expansion of the ring size at the daughter side, without apparent change in the total septin intensity. These data suggest that the AH-PH domains are essential for tethering the septin structures to the PM at the mother side during the HDR transition, and that the SID in Bud4-(AH-PH)Δ prefers to interact with septin structures formed during the HDR transition. Indeed, deletion of the SID, together with the AH-PH domains, in Bud4 [i.e. Bud4-(SID; AH-PH)Δ] completely abolished its localization to the bud neck and further destabilized the septin structure to almost non-detectable level during the HDR transition (Figures 6A and 6B). Together, these data indicate that the SID and AH-PH domains account for the entire neck-targeting signals in Bud4; and, more importantly, that while the SID can provide a means for Bud4-septin association, the AH-PH domains play a critical role in the HDR transition.

The localization of Bud3 increased slightly and appeared to co-shift with the septins from the mother side to the daughter side in *bud4-(AH-PH)Δ* cells during the HDR transition (Figure S7A, **arrows** and Figure S7B). This data suggests that Bud3 can associate with the septins independent of its interaction with Bud4 during the HDR transition. However, in contrast to Bud4-(AH-PH)Δ that associated with the single ring at the daughter side until the next budding event (Figure 6A, **asterisks**), Bud3 disappeared from the daughter side immediately after the HDR transition, despite the abundant presence of the septins (Figure S7A, **asterisks**). These data suggest that the maintenance of Bud3 in the septin double ring after the HDR transition depends on its interaction with Bud4. The disappearance of Bud3 from the daughter side occurred even more quickly in *bud4-(SID; AH-PH)Δ* cells than in *bud4-(AH-PH)Δ* cells (Figure S7A, **asterisks**). This is not surprising, as the septin structure disappeared much faster in *bud4-(SID; AH-PH)Δ* cells than in *bud4-(AH-PH)Δ* cells (Figures S7A and S7B). Collectively, these data suggest that the interaction between Bud3 and Bud4 as well as their interactions with the septins are highly regulated during the HDR transition, and that Bud4 can associate with the septin double ring (after the HDR transition) independent of its interaction with Bud3, whereas the association of Bud3 with the double ring depends on its interaction with Bud4.

Because all the analyses described above point to a critical role of the AH-PH domains of Bud4 in controlling Bud3 localization as well as septin organization during and after the HDR transition, we examined the architecture of the transitional hourglass in *bud4-(AH-PH)Δ* cells. Strikingly, these cells either failed to form circumferential single filaments completely (56 out of 78 structures examined) or formed asymmetrically (22 out of 78 structures examined) (Figure 6C) in the transitional hourglass, similar to the *bud4Δ* cells (Figure 3A). These data indicate that the AH-PH domains of Bud4 are most critical for its role in the assembly and maintenance of the transitional hourglass.

Discussion

In this study, we have defined a striking zonal architecture for the transitional hourglass with unparalleled resolution, which has direct implication on how two crucial cytokinetic structures – the septin double ring and the AMR - are simultaneously generated with a defined spatial relationship during the HDR transition (Figure 7). PREM analysis coupled

with immunogold labeling of Bud3 and Bud4 allowed us to visualize clearly the distinct zones of the transitional hourglass. The gauze-like structure is limited to the outer zones that consist of the longitudinal paired filaments, circumferential single filaments, Bud3, and Bud4, whereas the middle zone is occupied by the longitudinal paired filaments and circumferential myosin-II filaments. This zonal architecture suggests a mechanism by which the transitional hourglass is converted into a septin double ring that sandwiches the AMR. Previous studies suggest that the HDR transition, which is triggered by the mitotic exit network [10, 11, 46], must involve a net loss of septins from the division site [39, 40, 48], 90° change in filament orientation [40, 49], and the presence of spatial cues at the ends of the hourglass that instruct the double ring formation [15]. Based on this knowledge and the zonal architecture discovered in this study, we speculate that, during the HDR transition, the paired filaments in the transitional hourglass are triggered to disassemble into shorter fragments and/or septin complexes. Without the stabilization by Bud3 and Bud4 in the middle zone, the disassembled septins underneath the myosin-II filaments are lost, therefore, allowing the AMR to anchor to the PM and initiate its constriction. In the outer zones, the shorter septin filaments and/or complexes are stabilized at the PM through their binding to Bud3 and Bud4, and are then re-organized and/or re-polymerized into circumferential paired filaments that are connected to the circumferential single filaments via Bud3 and Bud4. Whether the single filaments also undergo dynamic rearrangement during the HDR transition remains unknown. Collectively, these dynamic actions in the outer zones lead to the formation of a septin double ring that sandwiches the AMR. Thus, the transitional hourglass pre-patterns two crucial cytokinetic structures that are known to act in concert to restrict diffusible factors at the division site during cytokinesis [30, 50].

We have also, for the first time, defined the critical roles of Bud3 and Bud4 in the HDR transition at the architecture and filament levels (Figure 7). The surprising finding is that Bud3 is absolutely essential for the assembly of the circumferential single filaments in the transitional hourglass, which presumably explains the fragmentation of septin structures during the HDR transition in *bud3Δ* cells. This role of Bud3 requires its interaction with Bud4 and septins, but not its RhoGEF activity towards Cdc42. On the other hand, Bud4 is required for the stability of the transitional hourglass and the double ring, especially at the mother side of the bud neck. PREM analysis suggests that Bud4 carries out this role, at least in part, by controlling the assembly and/or maintenance of both paired and single filaments in the transitional hourglass, and this function requires its conserved AH-PH domains, which also mediate its interaction with Bud3 [34, 35]. Taken together, these observations suggest that the interaction between Bud3 and Bud4 is essential for the assembly of the transitional hourglass and its subsequent remodeling into a double ring.

At the molecular level, we found that Bud4 is required for the formation of a bulky-looking cross-linker that connects septin filaments in the double ring at the interval of a septin octamer. This crosslinking presumably can occur between paired and single filaments as well as between neighboring paired filaments (e.g. in *bud3Δ* cells). Based on this observation, we hypothesize that the Bud4-Bud3 complex stabilizes the junction between the paired and single filaments in the transitional hourglass with Bud4 being more proximal to the paired filaments while Bud3 being more proximal to the single filaments (Figure 7). This model is also supported by the observation that Bud4 interacts with both Cdc11 and Shs1,

the terminal subunits for the two distinct septin octamers in budding yeast [36, 51]. Cdc11 octamers are known to form paired filaments in vitro [52] whereas Shs1 octamers cannot form linear filaments via end-to-end ligation but can be laterally staggered to form a ring-like structure or associate with Cdc11 octamer-formed filaments in vitro [53]. In addition, Cdc11 and Shs1 interact with each other [54–56]. Thus, the junction between the paired and single filaments in the transitional hourglass is likely defined by the Cdc11-Shs1 interaction and possibly other interactions involving either or both septins [15]. It's noteworthy that, in our model, the Shs1 octamers do not polymerize end-to-end into single filaments, and the detailed interactions between Bud3, Bud4, and the septins require further investigation.

Why is the mother side of the transitional hourglass or double ring preferentially disassembled in *bud4Δ* cells? One possibility is that the septins at the mother side of the bud neck are asymmetrically modified, e.g. by sumoylation [57] (Figure 7) to alter the interactions between Bud4 and the septins, membrane lipids, or Bud3 to enable a more rapid disassembly of the mother side of the transitional hourglass or double ring. Regardless of the molecular details, this mechanism must be evolved to accommodate the lifestyle of asymmetric cell division by the budding yeast, i.e. the mother cell is significantly larger than the daughter cell at the time of cytokinesis. Consequently, the mother cell enters the next cell cycle right after cytokinesis and cell separation, and disassembles the old septin ring at the division site and forms a new ring at an adjacent budding site much quicker than the daughter cell does.

As exemplified by the Bud3-Bud4 pair in budding yeast, a RhoGEF-anillin module is also likely involved in the coordination of cytokinesis and septin remodeling in fission yeast [12, 13, 58, 59], filamentous fungi [22, 23, 60], Drosophila [19], and mammalian cells [16–18, 28]. Further studies are required to establish to what extent the mechanisms underlying the RhoGEF and anillin-mediated septin remodeling during cytokinesis are conserved across model systems.

STAR METHODS

LEAD CONTACT AND MATERIALS AVAILABILITY

Further information and requests for research materials may be directed to and will be fulfilled by the Lead Contact, Erfei Bi (ebi@pennmedicine.upenn.edu). Reagents generated in this study will be made available on request.

EXPERIMENTAL MODEL AND SUBJECT DETAILS

Our experimental model is the budding yeast *Saccharomyces cerevisiae*. All yeast strains used in this study are listed in Table S1. Standard culture media and genetic techniques were used. Yeast strains were grown routinely at 25°C in synthetic complete (SC) minimal medium lacking specific amino acid(s) and/or uracil or in rich medium YM-1 or yeast extract/peptone/dextrose (YPD). New strains were constructed either by integrating a plasmid carrying a modified gene at a genomic locus or by transferring a deletion or tagged allele of a gene from one strain to another via PCR amplification and yeast transformation (see footnotes in Table S1).

METHOD DETAILS

Plasmids—All primers were purchased from Integrated DNA Technologies and described in Table S2. Sequencing of constructs was performed at the DNA Sequencing Facility, University of Pennsylvania. Plasmids YIp128-CDC3-GFP [48] and YIp128-CDC3-mCherry [61] (integrative, *LEU2*) carries an N-terminally GFP- or mCherry-tagged *CDC3* under the control of its own promoter, respectively. Plasmids pHIS3p::mRuby2-Tub1+3'UTR::URA3 and pHIS3p::mRuby2-Tub1+3'UTR::HPH [62], pFA6a-link-yEGFP-SpHis5 and pFA6a-link-yEGFP-Kan [64], and pFA6a-His3MX6 [65] were described previously. Plasmid YCp50-MYO1 (*CEN URA3*; supplied by S. Brown, University of Michigan, Ann Arbor, MI) carries wild-type *MYO1* under its own promoter control [66]. Plasmid pAG25 (*NatMX*6) [67] was purchased from Addgene and was used for making *myo1Δ::NAT* deletion.

Live-cell imaging and quantitative analysis—For time-lapse microscopy, cells were grown at 25°C to exponential phase in liquid SC media with selection for the presence or absence of specific plasmids carried in the yeast strain. Cells were concentrated by centrifugation, spotted onto a poly-lysine-coated glass-bottom dish, and then embedded with SC containing agarose [68]. SC media was added to dish for live imaging at room temperature (~23°C). Images were acquired using a Nikon microscope (model Eclipse Ti-U, Tokyo, Japan) equipped with a Nikon 100x/1.49NA oil objective (model CFI Apo TIRF 100x), and a Yokogawa spinning-disk confocal scanner unit (model CSU-X1, Tokyo, Japan). A Photometrics QuantEM EMCCD camera (model 512SC, Tucson, AZ, USA) was used for image capture. Solid-state lasers for excitation (488 nm for GFP and 561 nm for RFP) were housed in a launch constructed by Spectral Applied Research (model ILE-400, Richmond Hill, Ontario, Canada). The imaging system was controlled by MetaMorph version 7.8.10.0 (Molecular Devices, Downingtown, PA, USA). Images were taken with z-stacks of 11 × 0.7 μm for all the experiments.

For quantification of the fluorescence intensity of targeted protein-GFP signal (Bud3-GFP, Bud4-GFP, Cdc3-GFP, and Myo1-GFP, respectively), a sum projection was created and quantification was performed with ImageJ (National Institutes of Health). A polygon was drawn around the region of interest and the integrated density was measured. The fluorescence intensity of the background was subtracted from this measurement (outside the cell unless indicated otherwise). The data was further calculated as intensity per unit area, and finally normalized to the peak intensity (100%) of the protein-GFP signal at the bud neck in the cell. Data were analyzed with Microsoft Excel, and expressed as the mean value ± standard deviation (SD). For calculating the decrease in fluorescence intensity of a full-length protein (Bud3-GFP or Bud4-GFP) in a mutant (*bud3Δ* or *bud4Δ* cells) versus WT at the bud neck before the HDR transition, we use the formula of 1-(protein-GFP in mutant/protein-GFP in WT at the time point −14). For calculating the decrease in fluorescence intensity of a truncated protein [e.g. Bud4-(AH-PH)Δ-GFP] versus the full-length protein (e.g. Bud4-GFP) at the bud neck before and during the HDR transition, we use the formula of 1-(truncated protein-GFP/full-length protein-GFP) at the time points −14 and +4, respectively (see plots in relevant figures).

For imaging with VT-iSIM, cell growth and slide preparation was the same as described above. Images were acquired using an Olympus microscope (model Olympus IX71 inverted microscope) equipped with an Olympus 100x/1.4 NA U Plan-S-Apo oil immersion objective (Olympus America, Inc, Center Valley, PA), and a confocal scan head: VisiTech VT-iSIM (VisiTech International, Inc., Sunderland, UK). The Hamamatsu ORCA Flash4.0 V3 sCMOS (model C13440–20CU, Hamamatsu USA, Bridgewater NJ) and the Evolve® 512 Delta EMCCD Camera (Tucson, AZ, USA) were used for image capture. The imaging system was controlled by MetaMorph (Molecular Devices, Downingtown, PA, USA). For time-lapse imaging (Figure 1D), we took only one optical section per fluorophore per time point to avoid photo-bleaching. For snapshots (Figure 1E), images were taken with z-stacks of 21 × 0.25 μm.

For deconvolving the VT-iSIM images, we used the Microvolution deconvolution plugin of ImageJ [63].

Cell synchronization, spheroplasting, and unroofing—Cells of different strains containing the *cdc15*-2 mutation were cultured in 50 mL YM-1 medium with shaking at 25°C to achieve OD_{600} = 0.4. Cells were then pelleted and resuspended in 37°C-preheated YM-1 medium. Cells were grown at 37°C for 2.5 h to achieve synchrony at onset of cytokinesis or followed by down shifting to 25°C for 35 min to achieve synchrony at the double-ring stage.

Cells were washed with 40 mM Tris-EDTA (TE) (pH 8.0), and then incubated in 3 mL TE plus 5 μL β-Mercaptoethanol for 15 min at 30°C. After centrifugation, the cell pellet was resuspended in spheroplast buffer (10 mM PIPES,1.2 M sorbitol, pH 6.5) containing 0.3 mg/mL zymolyase-100T (Amsbio, Oxfordshire, UK) and incubated at 35°C with moderate shaking for 1 h. Sephroplasts were washed three times with the spheroplast buffer and then mounted to a polylysine-coated coverslip. Two coverslips with spheroplasts on top were dipped into the spheroplast buffer and 1X KHMgE buffer (70 mM KCl, 20 mM HEPES, 5 mM $MgCl_2$, 3 mM EGTA) sequentially, and then pressed against each other with the spheroplasts in between the coverslips on a slide with one drop of the 1X KHMgE buffer. The coverslips were lifted and then fixed immediately in 2% glutaraldehyde in 1X KHMgE buffer at room temperature (RT ≈ 23°C) for 20 min.

Immunogold labeling—The coverslips with fixed unroofed spheroplasts were quenched in 2 mg/mL and 5 mg/mL NaBH4 in phosphate-buffered saline (PBS) for 10 min sequentially, blocked in 1% glycine for 10 min, and then washed three times in PBS. The coverslips were blocked in PBS with 5% donkey serum for 30 min. Each coverslip was incubated with the goat polyclonal anti-GFP antibody (1:50 in PBS with 5% donkey serum, ABCAM ab5450) at RT for 1.5 h. After washing five times with PBS and blocking for 10 min in immunogold-labeling buffer (20 mM Tris-HCl, pH 8.0, 0.5 M Nacl, and 0.05% Tween 20) containing 0.5% donkey serum, the coverslips were incubated with 18-nm Colloidal Gold AffiniPure Donkey Anti-Goat IgG (H+L) (Jackson ImmunoResearch Laboratories, Inc. 705-215-147, 1:5 dilution) in immnogold-labeling buffer containing 5% donkey serum at RT for overnight. After washing five times in immunogold-labeling buffer

containing 0.05% donkey serum, the coverslips were fixed with 2% glutaraldehyde in 0.1 M sodium cacodylate, pH 7.3.

Critical point drying and platinum coating—This was done by following a protocol described previously [15, 69]. The coverslips with fixed unroofed spheroplasts were treated in 0.1% tannic acid in water for 20 min. After washing three times with water, they were stained in 0.2% uranyl acetate in water for 20 min, which was followed by sequential incubation in 10, 20, 40, 60, 80, 100% ethanol and then critical point-dried with Samdri PVT-3D (Tousimis) CPD. Platinum was rotary-shadowed to the samples at 45° angle to form ~2-nm layer and carbon was then rotary-shadowed at 90° angle to form a 3.5–4 nm layer.

PREM imaging and analysis—After detaching the glass coverslips with hydrofluoric acid, coated samples were mounted on EM grids and imaged using a JEM 1011 transmission electron microscope (JEOL USA, Peabody, MA) operated at 100 kV. Images were captured with an ORIUS 832.10W charge-coupled device (CCD) camera (Gatan, Warrendale, PA), and were presented in inverted contrast. Structures of interest were color-labeled using the Adobe Photoshop.

QUANTIFICATION AND STATISTICAL ANALYSIS

Quantification of fluorescence intensity was performed using NIH ImageJ. Data were analyzed with Microsoft Excel, and expressed as the mean value ± standard deviation (SD) throughout this study. Detailed statistical information can be found in Figures and Figure Legends.

DATA AND CODE AVAILABILITY

Data supporting the findings of this study are available within the paper and its Supplemental Information files and from the authors upon request.

Supplementary Material

Refer to Web version on PubMed Central for supplementary material.

ACKNOWLEDGMENTS

We thank Satoshi Okada and Yogini Bhavsar-Jog for initiating this project, John Pringle for yeast strains, Susan Brown and Wei-Lih Lee for plasmids, Andrea Stout of the CDB Imaging Core for assistance with light microscopy, Nadia Efmova, Maria Shutova, and Changsong Yang for assistance with EM, Joseph Marquardt, Katy Ong, and Hiroki Okada for critically reading the manuscript. This work was supported by NIH grants GM116876 (to E.B.) and GM095977 (to T.S.).

REFERENCES

1. Gladfelter AS, Pringle JR, and Lew DJ (2001). The septin cortex at the yeast mother-bud neck. Curr. Opin. Microbiol 4, 681–689. [PubMed: 11731320]
2. McMurray MA, and Thorner J (2009). Septins: molecular partitioning and the generation of cellular asymmetry. Cell Div. 4, 18. [PubMed: 19709431]
3. Caudron F, and Barral Y (2009). Septins and the lateral compartmentalization of eukaryotic membranes. Dev. Cell 16, 493–506. [PubMed: 19386259]

4. Oh Y, and Bi E (2011). Septin structure and function in yeast and beyond. Trends Cell Biol. 21, 141–148. [PubMed: 21177106]
5. Dolat L, Hu Q, and Spiliotis ET (2014). Septin functions in organ system physiology and pathology. Biol. Chem 395, 123–141. [PubMed: 24114910]
6. Marquardt J, Chen X, and Bi E (2019). Architecture, remodeling, and functions of the septin cytoskeleton. Cytoskeleton (Hoboken) 76, 7–14. [PubMed: 29979831]
7. Krokowski S, Lobato-Marquez D, Chastanet A, Pereira PM, Angelis D, Galea D, Larrouy-Maumus G, Henriques R, Spiliotis ET, Carballido-Lopez R, et al. (2018). Septins recognize and entrap dividing bacterial cells for delivery to lysosomes. Cell Host Microbe 24, 866–874 e864. [PubMed: 30543779]
8. Pfanzelter J, Mostowy S, and Way M (2018). Septins suppress the release of vaccinia virus from infected cells. J. Cell Biol 217, 2911–2929. [PubMed: 29921601]
9. Kim HB, Haarer BK, and Pringle JR (1991). Cellular morphogenesis in the *Saccharomyces cerevisiae* cell cycle: localization of the *CDC3* gene product and the timing of events at the budding site. J. Cell Biol 112, 535–544. [PubMed: 1993729]
10. Lippincott J, Shannon KB, Shou W, Deshaies RJ, and Li R (2001). The Tem1 small GTPase controls actomyosin and septin dynamics during cytokinesis. J. Cell Sci 114, 1379–1386. [PubMed: 11257003]
11. Cid VJ, Adamikova L, Sanchez M, Molina M, and Nombela C (2001). Cell cycle control of septin ring dynamics in the budding yeast. Microbiology 147, 1437–1450. [PubMed: 11390675]
12. Berlin A, Paoletti A, and Chang F (2003). Mid2p stabilizes septin rings during cytokinesis in fission yeast. J. Cell Biol 160, 1083–1092. [PubMed: 12654901]
13. Tasto JJ, Morrell JL, and Gould KL (2003). An anillin homologue, Mid2p, acts during fission yeast cytokinesis to organize the septin ring and promote cell separation. J. Cell Biol 160, 1093–1103. [PubMed: 12668659]
14. Estey MP, Di Ciano-Oliveira C, Froese CD, Bejide MT, and Trimble WS (2010). Distinct roles of septins in cytokinesis: SEPT9 mediates midbody abscission. J. Cell Biol 191, 741–749. [PubMed: 21059847]
15. Ong K, Wloka C, Okada S, Svitkina T, and Bi E (2014). Architecture and dynamic remodelling of the septin cytoskeleton during the cell cycle. Nat. Commun 5, 5698. [PubMed: 25474997]
16. Renshaw MJ, Liu J, Lavoie BD, and Wilde A (2014). Anillin-dependent organization of septin filaments promotes intercellular bridge elongation and Chmp4B targeting to the abscission site. Open Biol. 4, 130190–130190. [PubMed: 24451548]
17. Wang K, Wloka C, and Bi E (2019). Non-muscle myosin-II is required for the generation of a constriction site for subsequent abscission. iScience 13, 69–81. [PubMed: 30825839]
18. Karasmanis EP, Hwang D, Nakos K, Bowen JR, Angelis D, and Spiliotis ET (2019). A septin double ring controls the spatiotemporal organization of the ESCRT machinery in cytokinetic abscission. Curr. Biol 29, 2174–2187. [PubMed: 31204162]
19. Hickson GR, and O'Farrell PH (2008). Rho-dependent control of anillin behavior during cytokinesis. J. Cell Biol 180, 285–294. [PubMed: 18209105]
20. Justa-Schuch D, Heilig Y, Richthammer C, and Seiler S (2010). Septum formation is regulated by the *RHO4*-specific exchange factors *BUD3* and *RGF3* and by the landmark protein *BUD4* in *Neurospora crassa*. Mol. Microbiol 76, 220–235. [PubMed: 20199606]
21. Berepiki A, and Read ND (2013). Septins are important for cell polarity, septation and asexual spore formation in *Neurospora crassa* and show different patterns of localisation at germ tube tips. PLoS One 8, e63843. [PubMed: 23691103]
22. Westfall PJ, and Momany M (2002). *Aspergillus nidulans* septin AspB plays pre- and postmitotic roles in septum, branch, and conidiophore development. Mol. Biol. Cell 13, 110–118. [PubMed: 11809826]
23. Si H, Rittenour WR, Xu K, Nicksarlian M, Calvo AM, and Harris SD (2012). Morphogenetic and developmental functions of the *Aspergillus nidulans* homologues of the yeast bud site selection proteins Bud4 and Axl2. Mol. Microbiol 85, 252–270. [PubMed: 22651396]
24. Straight AF, Field CM, and Mitchison TJ (2005). Anillin binds nonmuscle myosin II and regulates the contractile ring. Mol. Biol. Cell 16, 193–201. [PubMed: 15496454]

25. Piekny AJ, and Glotzer M (2008). Anillin is a scaffold protein that links RhoA, actin, and myosin during cytokinesis. Curr. Biol 18, 30–36. [PubMed: 18158243]
26. Hickson GR, and O'Farrell PH (2008). Anillin: a pivotal organizer of the cytokinetic machinery. Biochem. Soc. Trans 36, 439–441. [PubMed: 18481976]
27. Piekny AJ, and Maddox AS (2010). The myriad roles of anillin during cytokinesis. Semin. Cell Dev. Biol 21, 881–891. [PubMed: 20732437]
28. Frenette P, Haines E, Loloyan M, Kinal M, Pakarian P, and Piekny A (2012). An anillin-Ect2 complex stabilizes central spindle microtubules at the cortex during cytokinesis. PLoS One 7, e34888. [PubMed: 22514687]
29. Kang PJ, Lee ME, and Park HO (2014). Bud3 activates Cdc42 to establish a proper growth site in budding yeast. J. Cell Biol 206, 19–28. [PubMed: 25002677]
30. Wloka C, Nishihama R, Onishi M, Oh Y, Hanna J, Pringle JR, Krauss M, and Bi E (2011). Evidence that a septin diffusion barrier is dispensable for cytokinesis in budding yeast. Biol. Chem 392, 813–829. [PubMed: 21824009]
31. Chant J, Mischke M, Mitchell E, Herskowitz I, and Pringle JR (1995). Role of Bud3p in producing the axial budding pattern of yeast. J. Cell Biol 129, 767–778. [PubMed: 7730410]
32. Sanders SL, and Herskowitz I (1996). The Bud4 protein of yeast, required for axial budding, is localized to the mother/bud neck in a cell cycle-dependent manner. J. Cell Biol 134, 413–427. [PubMed: 8707826]
33. Guo J, Gong T, and Gao XD (2011). Identification of an amphipathic helix important for the formation of ectopic septin spirals and axial budding in yeast axial landmark protein Bud3p. PLoS One 6, e16744. [PubMed: 21408200]
34. Kang PJ, Hood-DeGrenier JK, and Park HO (2013). Coupling of septins to the axial landmark by Bud4 in budding yeast. J. Cell Sci 126, 1218–1226. [PubMed: 23345395]
35. Wu H, Guo J, Zhou YT, and Gao XD (2015). The anillin-related region of Bud4 is the major functional determinant for Bud4's function in septin organization during bud growth and axial bud site selection in budding yeast. Eukaryot. Cell 14, 241–251. [PubMed: 25576483]
36. Finnigan GC, Duvalyan A, Liao EN, Sargsyan A, and Thorner J (2016). Detection of protein-protein interactions at the septin collar in *Saccharomyces cerevisiae* using a tripartite split-GFP system. Mol. Biol. Cell 27, 2708–2725. [PubMed: 27385335]
37. Eluere R, Varlet I, Bernadac A, and Simon MN (2012). Cdk and the anillin homolog Bud4 define a new pathway regulating septin organization in yeast. Cell Cycle 11, 151–158. [PubMed: 22185758]
38. McQuilken M, Jentzsch MS, Verma A, Mehta SB, Oldenbourg R, and Gladfelter AS (2017). Analysis of septin reorganization at cytokinesis using polarized fluorescence microscopy. Front. Cell Dev. Biol 5, 42–42. [PubMed: 28516085]
39. Dobbelaere J, Gentry MS, Hallberg RL, and Barral Y (2003). Phosphorylation-dependent regulation of septin dynamics during the cell cycle. Dev. Cell 4, 345–357. [PubMed: 12636916]
40. DeMay BS, Bai X, Howard L, Occhipinti P, Meseroll RA, Spiliotis ET, Oldenbourg R, and Gladfelter AS (2011). Septin filaments exhibit a dynamic, paired organization that is conserved from yeast to mammals. J. Cell Biol 193, 1065–1081. [PubMed: 21670216]
41. Chen H, Howell AS, Robeson A, and Lew DJ (2011). Dynamics of septin ring and collar formation in *Saccharomyces cerevisiae*. Biol. Chem 392, 689–697. [PubMed: 21736496]
42. Wloka C, Vallen EA, Thé L, Fang X, Oh Y, and Bi E (2013). Immobile myosin-II plays a scaffolding role during cytokinesis in budding yeast. J. Cell Biol 200, 271–286. [PubMed: 23358243]
43. Lord M, Yang MC, Mischke M, and Chant J (2000). Cell cycle programs of gene expression control morphogenetic protein localization. J. Cell Biol 151, 1501–1512. [PubMed: 11134078]
44. Bi E, Maddox P, Lew DJ, Salmon ED, McMillan JN, Yeh E, and Pringle JR (1998). Involvement of an actomyosin contractile ring in *Saccharomyces cerevisiae* cytokinesis. J. Cell Biol 142, 1301–1312. [PubMed: 9732290]
45. Lippincott J, and Li R (1998). Sequential assembly of myosin II, an IQGAP-like protein, and filamentous actin to a ring structure involved in budding yeast cytokinesis. J. Cell Biol 140, 355–366. [PubMed: 9442111]

46. Tamborrini D, Juanes MA, Ibanes S, Rancati G, and Piatti S (2018). Recruitment of the mitotic exit network to yeast centrosomes couples septin displacement to actomyosin constriction. Nat. Commun 9, 4308. [PubMed: 30333493]
47. Kang PJ, Angerman E, Jung CH, and Park HO (2012). Bud4 mediates the cell-type-specific assembly of the axial landmark in budding yeast. J. Cell Sci 125, 3840–3849. [PubMed: 22553209]
48. Caviston JP, Longtine M, Pringle JR, and Bi E (2003). The role of Cdc42p GTPase-activating proteins in assembly of the septin ring in yeast. Mol. Biol. Cell 14, 4051–4066. [PubMed: 14517318]
49. Vrabioiu AM, and Mitchison TJ (2006). Structural insights into yeast septin organization from polarized fluorescence microscopy. Nature 443, 466–469. [PubMed: 17006515]
50. Dobbelaere J, and Barral Y (2004). Spatial coordination of cytokinetic events by compartmentalization of the cell cortex. Science 305, 393–396. [PubMed: 15256669]
51. Gavin AC, Aloy P, Grandi P, Krause R, Boesche M, Marzioch M, Rau C, Jensen LJ, Bastuck S, Dumpelfeld B, et al. (2006). Proteome survey reveals modularity of the yeast cell machinery. Nature 440, 631–636. [PubMed: 16429126]
52. Frazier JA, Wong ML, Longtine MS, Pringle JR, Mann M, Mitchison TJ, and Field C (1998). Polymerization of purified yeast septins: evidence that organized filament arrays may not be required for septin function. J. Cell Biol 143, 737–749. [PubMed: 9813094]
53. Garcia G 3rd, Bertin A, Li Z, Song Y, McMurray MA, Thorner J, and Nogales E (2011). Subunit-dependent modulation of septin assembly: budding yeast septin Shs1 promotes ring and gauze formation. J. Cell Biol 195, 993–1004. [PubMed: 22144691]
54. Mortensen EM, McDonald H, Yates J 3rd, and Kellogg DR (2002). Cell cycle-dependent assembly of a Gin4-septin complex. Mol. Biol. Cell 13, 2091–2105. [PubMed: 12058072]
55. Versele M, Gullbrand B, Shulewitz MJ, Cid VJ, Bahmanyar S, Chen RE, Barth P, Alber T, and Thorner J (2004). Protein-protein interactions governing septin heteropentamer assembly and septin filament organization in *Saccharomyces cerevisiae*. Mol. Biol. Cell 15, 4568–4583. [PubMed: 15282341]
56. Farkasovsky M, Herter P, Voss B, and Wittinghofer A (2005). Nucleotide binding and filament assembly of recombinant yeast septin complexes. Biol. Chem 386, 643–656. [PubMed: 16207085]
57. Johnson ES, and Blobel G (1999). Cell cycle-regulated attachment of the ubiquitin-related protein SUMO to the yeast septins. J. Cell Biol 147, 981–993. [PubMed: 10579719]
58. Munoz S, Manjon E, and Sanchez Y (2014). The putative exchange factor Gef3p interacts with Rho3p GTPase and the septin ring during cytokinesis in fission yeast. J. Biol. Chem 289, 21995–22007. [PubMed: 24947517]
59. Wang N, Wang M, Zhu YH, Grosel TW, Sun D, Kudryashov DS, and Wu JQ (2015). The Rho-GEF Gef3 interacts with the septin complex and activates the GTPase Rho4 during fission yeast cytokinesis. Mol. Biol. Cell 26, 238–255. [PubMed: 25411334]
60. Si H, Justa-Schuch D, Seiler S, and Harris SD (2010). Regulation of septum formation by the Bud3-Rho4 GTPase module in *Aspergillus nidulans*. Genetics 185, 165–176. [PubMed: 20176976]
61. Gao XD, Sperber LM, Kane SA, Tong Z, Hin Yan Tong A, Boone C, and Bi E (2007). Sequential and distinct roles of the cadherin domain-containing protein Axl2p in cell polarization in yeast cell cycle. Mol. Biol. Cell 18, 2542–2560. [PubMed: 17460121]
62. Markus SM, Omer S, Baranowski K, and Lee WL (2015). Improved plasmids for fluorescent protein tagging of microtubules in *Saccharomyces cerevisiae*. Traffic 16, 773–786. [PubMed: 25711127]
63. Schindelin J, Arganda-Carreras I, Frise E, Kaynig V, Longair M, Pietzsch T, Preibisch S, Rueden C, Saalfeld S, Schmid B, et al. (2012). Fiji: an open-source platform for biological-image analysis. Nat. Methods 9, 676–682. [PubMed: 22743772]
64. Sheff MA, and Thorn KS (2004). Optimized cassettes for fluorescent protein tagging in *Saccharomyces cerevisiae*. Yeast 21, 661–670. [PubMed: 15197731]
65. Longtine MS, McKenzie A III,, DeMarini DJ, Shah NG, Wach A, Brachat A, Philippsen P, and Pringle JR (1998). Additional modules for versatile and economical PCR-based gene deletion and modification in *Saccharomyces cerevisiae*. Yeast 14, 953–961. [PubMed: 9717241]

66. Vallen EA, Caviston J, and Bi E (2000). Roles of Hof1p, Bni1p, Bnr1p, and Myo1p in cytokinesis in *Saccharomyces cerevisiae*. Mol. Biol. Cell 11, 593–611. [PubMed: 10679017]

67. Goldstein AL, and McCusker JH (1999). Three new dominant drug resistance cassettes for gene disruption in *Saccharomyces cerevisiae*. Yeast 15, 1541–1553. [PubMed: 10514571]

68. Okada S, Wloka C, and Bi E (2017). Analysis of protein dynamics during cytokinesis in budding yeast. Methods Cell Biol. 137, 25–45. [PubMed: 28065309]

69. Svitkina T (2016). Imaging cytoskeleton components by electron microscopy. Methods Mol. Biol 1365, 99–118. [PubMed: 26498781]

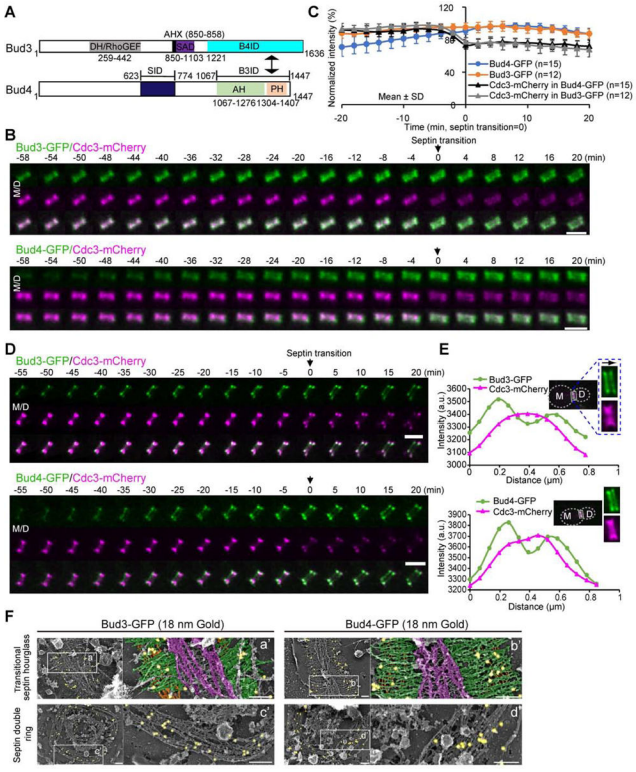

Figure 1. Bud3 and Bud4 localize to the outer zones of the transitional hourglass as well as the double ring

(A) Domains and motifs in Bud3 and Bud4, modified from references [33, 35]. DH/RhoGEF, Dbl Homology domain/Rho Guanine-nucleotide-Exchange Factor; AHX, Amphipathic Helix; SAD, Septin Association Domain; B4ID, Bud4-Interacting Domain; SID, Septin-Interacting Domain; AH, Anillin Homology; PH, Pleckstrin Homology; and B3ID, Bud3-Interacting Domain.

(B) Montage of time-lapse data showing the localizations of Bud3 and Bud4 in relation to the septins during the cell cycle. Cells of the strains YEF8459 (*BUD3-GFP CDC3-mCherry*) and YEF8461 (*BUD4-GFP CDC3-mCherry*) were imaged with a 2-min interval. Due to space limitation, only selected frames are shown here. Septin transition = time point “0” (the first time-point after the full drop in septin intensity). “D/M” refers to Daughter/Mother orientation throughout this paper. Scale bar, 2 μm. See also Figure S1 and Video S1.

(C) Quantitative analysis of Bud3 and Bud4 localization (Mean ± SD) in relation to septin HDR transition during the cell cycle. Imaging data acquired from (**B**) were used for this analysis. n, individual cells. Please note that max projection of a z-stack is used to illustrate the pattern of protein localization whereas sum projection of the same z-stack is used for the quantitative analysis throughout this study.

(D) Time-lapse analysis of Bud3 and Bud4 localization in relation to the septin hourglass and double ring by iSIM. Strains imaged were YEF8459 (*BUD3-GFP CDC3-mCherry*) and YEF8461 (*BUD4-GFP CDC3-mCherry*). Cdc3-mCherry: septin HDR transition was used as the clock. Due to photo-bleaching, a single optical section for each fluorophore was acquired for each time point to show the pattern of protein localization. Scale bar, 2 μm. See also Video S1.

(E) Line-scanning profiles of Bud3-GFP and Bud4-GFP in relation to the septin hourglass (Cdc3-mCherry) across the boxed region at the bud neck from representative cells of the same strains described in (**D**). Z-sections of the cells were imaged by iSIM and sum-projected into a 2D image that was subjected to line-scanning analysis. a.u., arbitrary units. (F) Immunogold labeling PREM analysis of Bud3 and Bud4 localization in relation to the septin transitional hourglass and double ring. Strains used were YEF8455 (*BUD3-GFP cdc15–2*) and YEF8457 (*BUD4-GFP cdc15–2*). The *cdc15–2* mutation was used to synchronize cells at the stage of transitional hourglass (top) or double ring (bottom). Unroofed cell cortices were first labeled with a primary anti-GFP antibody followed by an 18-nm gold particle conjugated secondary antibody (pseudo-colored in yellow). Myosin-II filaments (purple), paired filaments (green), and single filaments (orange) are indicated. Scale bar, 200 nm.

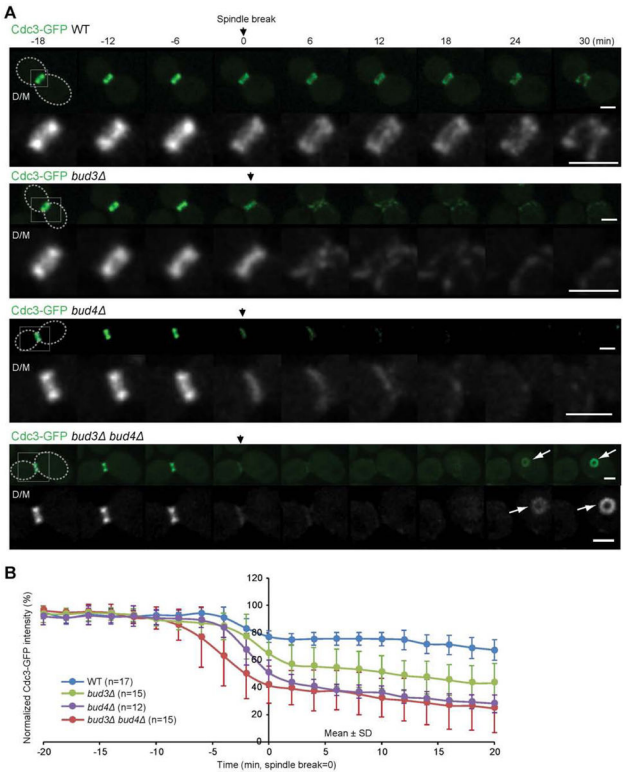

Figure 2. Bud3 and Bud4 are differentially required but collectively essential for the double ring assembly

(A) Time-lapse analysis of septin organization (Cdc3-GFP) during the cell cycle (mRuby2-Tub1) in WT (YEF8106), *bud3* (YEF8104), *bud4* (YEF8105) and *bud3 bud4* (YEF8103) cells. Cells were imaged with a 2-min interval, and only selected frames are shown here. The selected bud-neck region (white box) was magnified and shown in the bottom panel for each strain. “Spindle break” refers to the cell cycle-triggered breakage of the mitotic spindle at its mid-point. Scale bar, 2 μm. See also Video S2.

(B) The intensity of Cdc3-GFP at the bud neck from the cells imaged in (**A**) was quantified against the background outside the cell. Data are expressed as mean value ± SD.

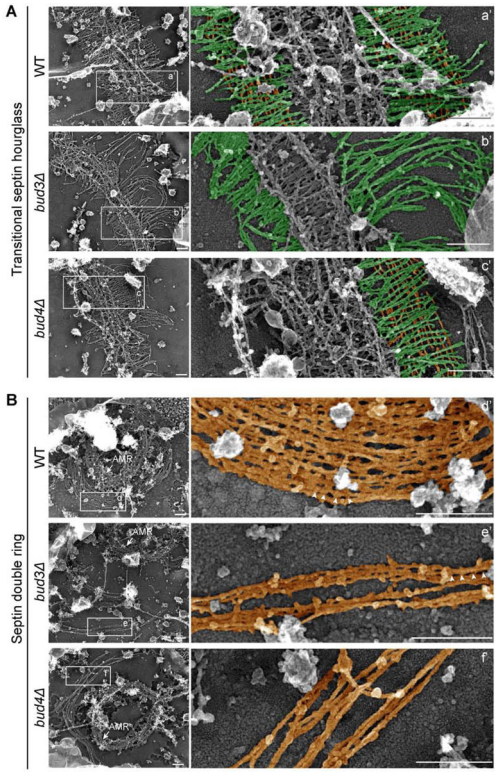

Figure 3. Bud3 and Bud4 play distinct roles in generating the architecture of the transitional hourglass and the double ring

(A) PREM analysis of the transitional hourglass in WT, *bud3Δ*, and *bud4Δ* cells. Cells of the strains YEF8356 (*cdc15–2*) (WT), YEF8909 (*bud3Δ cdc15–2*), and YEF8908 (*bud4Δ cdc15–2*) were synchronized at the stage of transitional hourglass and then processed for PREM analysis. To aid visualization and filament recognition, the paired filaments oriented along the mother-bud axis (green) and the circumferential single filaments (orange) in the enlarged regions of the transitional hourglasses from the WT (**a'**), *bud3Δ* (**b'**), and *bud4Δ* (**c'**) cells were highlighted. See also Figures S2A and S2B.

(B) PREM analysis of the double ring in WT, *bud3Δ*, and *bud4Δ* cells. The same strains as in (**A**) were used for the analysis except that the cells were synchronized at the double ring stage. A constricted actomyosin ring (AMR) within or next to the double ring or its fragments (only one side of the double ring was visualized) was indicated to illustrate the spatial relationship between the two cytokinetic structures, which also confirms the correctness of the cell cycle stage. To visualize the filament density and identify the Bud4-dependent "bulky-looking" cross-linker, the cross-linkers (white arrowheads) on the double-ring filaments (orange) in the enlarged regions of the structures from the WT (**d'**), *bud3Δ* (**e'**), and *bud4Δ* (**f'**) cells were highlighted. Scale bar, 200 nm. See also Figures S2C, S3, S4, and Video S3.

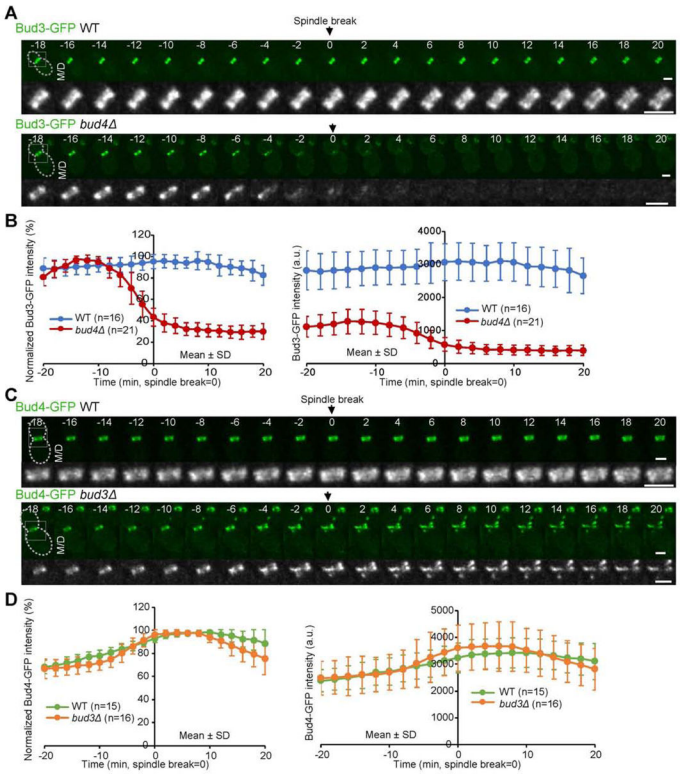

Figure 4. Bud3 targets to the division site via both Bud4-dependent and –independent mechanisms.

(A) Montage of time-lapse data showing the neck-localization dependence of Bud3 on Bud4 during the cell cycle. The strains imaged were YEF8408 in (WT) (top) and YEF8409 (*bud4*) (bottom). Cells were imaged with a 2-min interval, and only selected frames are shown here. Spindle break = time point "0" (arrowhead). Scale bar, 2 μm. See also Video S4.

(B) Quantitative analysis of Bud3 localization at the bud neck during the cell cycle. Both normalized intensity (left) and the raw data (right) acquired in (A) are presented to show the rate and level of Bud3 accumulation, respectively. Data are expressed as mean value ± SD. a.u., arbitrary units.

(C) Montage of time-lapse data showing the neck-organization dependence of Bud4 on Bud3 during the HDR transition. The strains imaged were YEF8410 in (WT) (top) and YEF8462 (*bud3*) (bottom). Cells were imaged with a 2-min interval, and only selected frames are shown here. Scale bar, 2 μm. See also Video S4.

(D) Quantitative analysis of Bud4 localization at the bud neck during the cell cycle. Both normalized intensity (left) and the raw data (right) acquired in (C) are presented to show the rate and level of Bud4 accumulation, respectively. Data are expressed as mean value ± SD. a.u., arbitrary units.

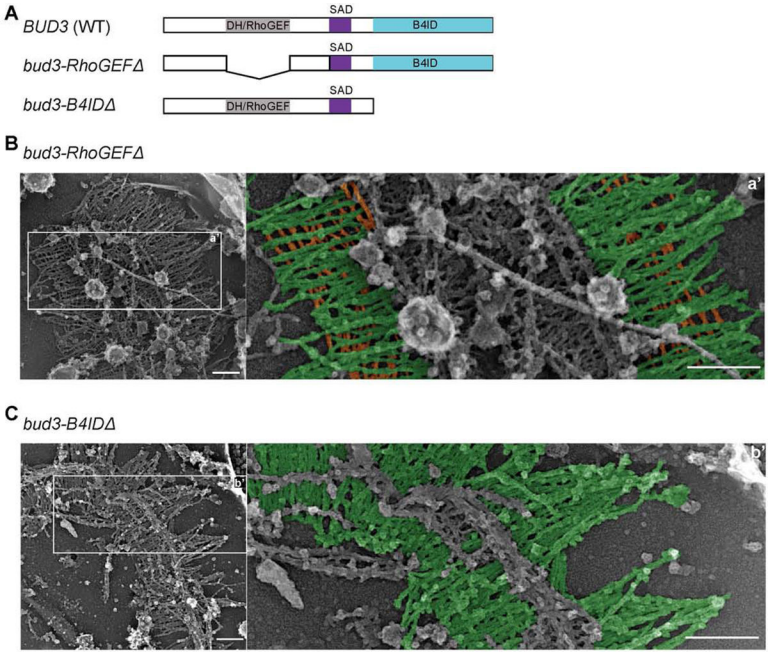

Figure 5. The Bud4-interacting domain, not the RhoGEF domain, of Bud3 is essential for the assembly of the circumferential single filaments in the transitional hourglass

(A) WT and mutant Bud3 constructs used in this analysis. DH/RhoGEF, Dbl Homology (DH) domain/Rho Guanine-nucleotide-Exchange Factor; SAD, Septin Association Domain; B4ID, Bud4-Interacting Domain.

(B) PREM analysis of the transitional hourglass from the strain YEF9672 (*bud3-RhoGEFΔcdc15-2*). See also Figure S5.

(C) PREM analysis of the transitional hourglass from the strain YEF9817 (*bud3-B4IDΔcdc15-2*). Scale bar, 200 nm. See also Figure S6.

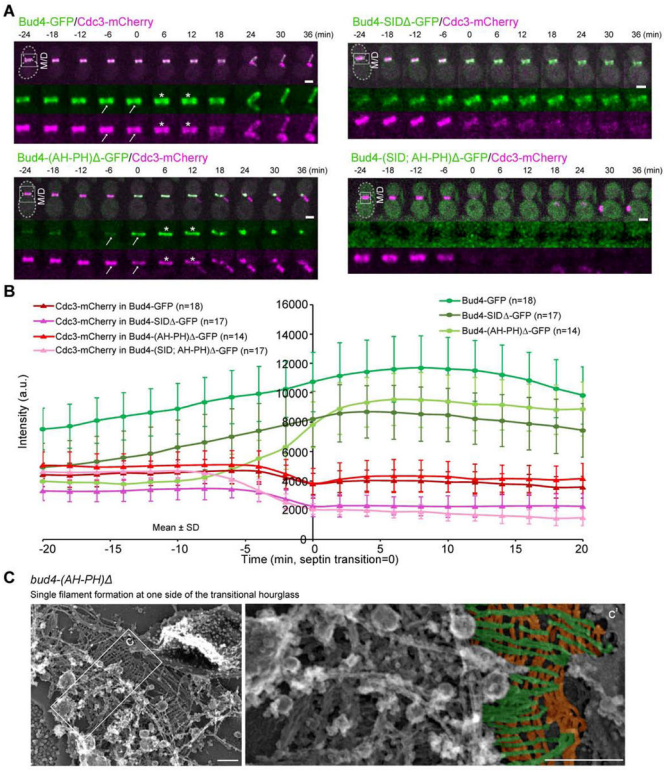

Figure 6. The AH-PH domains of Bud4 are critical for the assembly and stability of the transitional hourglass

(A) Montage of time-lapse data showing the neck localizations of Bud4, Bud4-SIDΔ, Bud4-(AH-PH)Δ, Bud4-(SID; AH-PH)Δ, in relation to the septins during the HDR transition. The strains imaged were YEF8461 (*BUD4-GFP CDC3-mCherry*), YEF10122 [*bud4-SIDΔ-GFP CDC3-mCherry*], YEF9520 [*bud4-(AH-PH)Δ-GFP CDC3-mCherry*], and YEF10124 [*bud4-(SID; AH-PH)Δ-GFP CDC3-mCherry*]. Cells were imaged with a 2-min interval, and only selected frames are shown here. Septin transition = time point "0". Scale bar, 2 μm.

(B) Quantitative analysis of the intensities of Bud4 variants and septin at the bud neck during the cell cycle. The data acquired in (**A)** are used for the analysis, and are expressed as mean value ± SD. a.u., arbitrary units. See also Figure S7.

(C) PREM analysis of the transitional hourglass from the strain YEF9523 [*bud4-(AH-PH)Δcdc15-2*]. Scale bar, 200 nm.

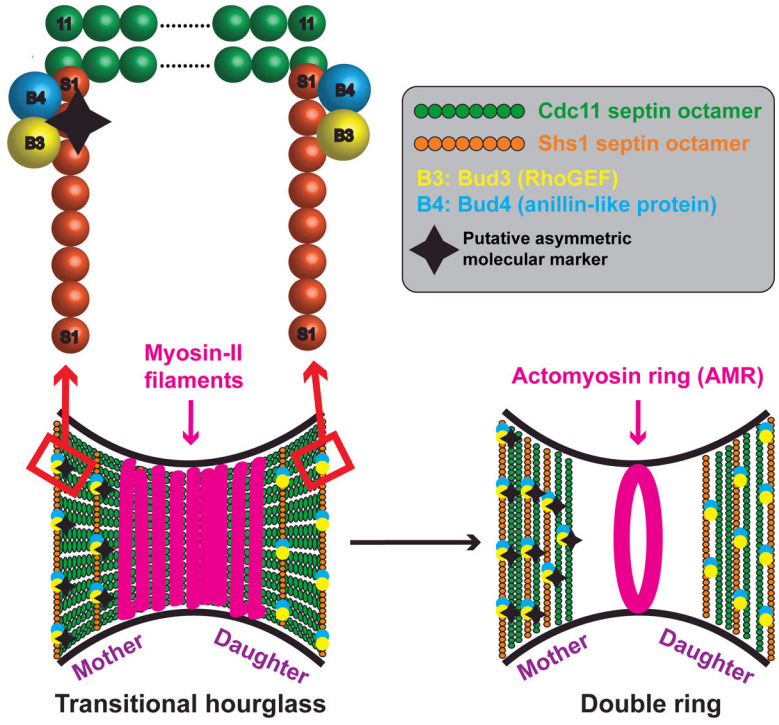

Figure 7. A model for the mechanism of Bud3- and Bud4-mediated septin architectural remodeling at the division site

Bud3 and Bud4 play distinct and essential roles in the assembly and remodeling of the transitional hourglass (see text for details)

KEY RESOURCES TABLE

REAGENT or RESOURCE	SOURCE	IDENTIFIER
Bacterial Strains		
E. coli strain DH5α	Invitrogen	Cat #: 18258012
Chemicals, Peptides, and Recombinant Proteins		
Bacto Tryptone	Formedium, Hunstanton, UK	Ca t#: TRP03
D(+)- Glucose-Monohydrat	Merck, Darmstadt, Germany	Cat #: 1.08342.2500
Yeast nitrogen base w.o. $(NH4)_2SO4$	Formedium, Hunstanton, UK	Cat #: CYN0502
L-Arginine 136,15N4 Hydrochloride	Sigma, Darmstadt, Germany	Cat #: 608033–250MG
L-Asparagine-Monohydrate	AppliChem, Darmstadt, Germany	Cat #: A3669,0100
L-Isoleucine	Ducheta Biochemie, Haarlem, NL	Cat #: IO 711.0100
L-Lysine-Monohyrate	Merck, Darmstadt, Germany	Cat #: 1.12233.0100
L-Methionine	Sigma, Darmstadt, Germany	Cat #: M9625
L-Phenylalanine	Ducheta Biochemie, Haarlem, NL	Cat #: P0716.0100
L-Threonine	Sigma, Darmstadt, Germany	Cat #: T-8625
Adenine	Sigma, Darmstadt, Germany	Cat #: A9126–100
L-Histidine	Ducheta Biochemie, Haarlem, NL	Cat #: H0720
L-Leucine	Ducheta Biochemie, Haarlem, NL	Cat #: L0712
Uracil	Sigma, Darmstadt, Germany	Cat #: U0750–100G
L-Tryptophane	Sigma, Darmstadt, Germany	Cat #: T-0254
Yeast extract powder (Yeast Bacto Extract)	Formedium, Hunstanton, UK	Cat #: YEA04
Agar-Agar	Carl Roth GmbH+Co. KG, Karlsruhe, Germany	Cat #:5210.5
5-fluoro-orotic acid	Formedium, Hunstanton, UK	Cat #: 5FOA10
Ampicilin Sodium	Formedium, Hunstanton, UK	Cat#: AMP100
Agarose	Sigma, Darmstadt, Germany	Cat #: A9539–500
G-418 Disulphate	Formedium, Hunstanton, UK	Cat #: G4185
PEG3000	Merck, Darmstadt, Germany	Cat #: 8.17019.5000
EDTA	AppliChem, Darmstadt, Germany	Cat #: APPCA3553.1000
Lithiumacetate	Carl Roth GmbH+Co. KG, Karlsruhe, Germany	Cat #: 5447.1
Sodium Chloride	Sigma, Darmstadt, Germany	Cat #: 31434
Zymolyase 100T	Amsbio, Oxfordshire, UK	Cat#: 120493–1
Glutaraldehyde	Polyscience, Pennsylvania, USA	Cat#: 01909–10
Anti-GFP antibody	Abcam, Cambridge, USA	Cat#: ab5450
18 nm Colloidal Gold AffiniPure Donkey Anti-Goat IgG (H+L)	Jackson ImmunoResearch, Pennsylvania, USA	Cat#: 705-215-147
Tannic Acid	Mallinckrodt, Kentucky, USA	Cat#:1764
Uranyl Acetate	Structure Probe, Pennsylvania, USA	Cat#:02624
Experimental Models: Organisms/Strains		
Saccharomyces cerevisiae strains, see Table S1	This paper	N/A
Oligonucleotides		

REAGENT or RESOURCE	SOURCE	IDENTIFIER
Primers, see Table S2	This paper	N/A
Recombinant DNA		
Plasmid: YIp128-CDC3-GFP	[48]	N/A
Plasmid: YIp128-CDC3-mCherry	[61]	N/A
Plasmid: pFA6a-TRP1	Addgene	Cat #: 41595
Plasmid: pAG25	Addgene	Cat #: 35121
Plasmid: pFA6a-URA3-KanMX6	John Pringle	N/A
Plasmid: pHIS3p: mRuby2-Tub1+3'UTR::HIS3	[62]	N/A
Plasmid: pHIS3p: mRuby2-Tub1+3'UTR::HPH	[62]	N/A
Plasmid: pFA6a- link-yoEGFP-Sp*HIS5*	Addgene	Cat #: 44836
Plasmid: pFA6a-link-yoEGFP-KAN	Addgene	Cat #: 44900
Software and Algorithms		
MetaMorph version 7.8.10.0	Molecular Devices	https://www.moleculardevices.com/
Fiji	[63]	https://imagej.net/Fiji/
NIH ImageJ (1.51j)	NIH	https://imagej.nih.gov/ij/